Solar Energy Materials & Solar Cells 295 (2026) 113943

Contents lists available at ScienceDirect

Solar Energy Materials and Solar Cells

journal homepage: www.elsevier.com/locate/solmat

Optimization of optical absorption and transport layer effects on Perovskite/ACIGS tandem solar cells

Nour El I. Boukortt [a,b,*], Antonio Garcia Loureiro [a], Johan Lauwaert [b]

[a] Centro Singular de Investigación en Tecnoloxías Intelixentes (CiTIUS), University of Santiago de Compostela, 15782, Santiago de Compostela, Spain
[b] Department of Electronics and Information Systems, Ghent University, Technology Park 126, Zwijnaarde, Belgium

ARTICLE INFO

Keywords:
Tandem
Tunneling
Interface
Light
Modeling

ABSTRACT

This study presents a comprehensive numerical investigation of two-terminal (2T) perovskite/ACIGS tandem solar cells using Silvaco TCAD tools, aiming to guide the design of high-efficiency tandem configuration. The subcells were calibrated based on data from experimentally fabricated perovskite and ACIGS devices, with a band-to-band tunneling junction employed to enable efficient carrier recombination. Despite successful stacking, the tandem configuration exhibits a V_{oc} loss of ~28 mV before subcells matching, attributed to interfacial limitations in the top subcell. To address this, we explored the interplay of optical transparency, defect passivation, and charge transport by (1) selecting perovskite materials with tailored optoelectronic properties and thickness profiles, and (2) optimizing the electron transport layer (ETL) to minimize interfacial trap density and enhance charge extraction. Our optimized tandem structure achieves a simulated power conversion efficiency of 30.71 %, with a J_{sc} of 18.51 mA/cm^2, a V_{oc} of 2.05 V, and an *FF* of 80.97 %. The device further demonstrates enhanced thermal stability, with improved temperature coefficients for voltage (−0.164 %K^{-1}), current (−3.85 × 10^{-6} % K^{-1}), and power (−0.183 %K^{-1}), outperforming baseline models and silicon references. Comparative benchmarking confirms the effectiveness of the proposed strategy. This work not only advances predictive modeling of tandem photovoltaics but also offers actionable insights for overcoming interfacial and optical bottlenecks, paving the way for next-generation high-performance solar technologies.

1. Introduction

In recent years, thin-film solar cells have garnered significant attention due to their low cost and high-power conversion efficiency (PCE, η) [1]. Among these, single-junction lead halide perovskite solar cells (PSCs) have made remarkable advancements, achieving a PCE of 27 % [2,3], thanks to their exceptional optoelectronic properties, including high absorption coefficients and diffusion lengths [4,5]. However, the carrier mobility in perovskite remains lower and less stable compared to silicon, where electron and hole mobilities are μ_n = 1111 cm^2/V.s and μ_p = 421.6 cm^2/V.s, respectively [6,7]. Single-junction cells are limited by fundamental efficiency constraints, such as the inability to absorb low-energy photons and the thermalization losses of high-energy photons [8,9].

Tandem solar cells (TSCs), which stack subcells with different bandgaps, overcome the efficiency limitations of single-junction devices by capturing a broader portion of the solar spectrum more effectively. This enables them to surpass the 33 % Shockley–Queisser efficiency limit of single-junction solar cells [10–12]. Perovskite-based tandem solar cells, in particular, show great promise for future solar power generation due to their tunable bandgap and high-power conversion efficiency [13,14]. Although tandems can offer a lower cost per watt thanks to their superior efficiency, their overall fabrication cost remains higher than that of single-junction solar cells [15,16]. This is primarily due to the added complexity of materials and processing, the inclusion of additional layers (such as top cells and interconnection layers like tunnel recombination junctions), and potential yield and reliability issues during the early stages of commercialization.

Notable configurations include perovskite/silicon (PSC/Si) cells, which have achieved a certified PCE of 34.6 % [2], and perovskite/CIGS (PSC/CIGS) cells, which offer distinct advantages such as flexibility, lightweight form factor, and superior suitability for space and indoor applications due to their remarkable radiation resistance retaining over 85 % of their initial efficiency after exposure to 68 MeV protons at a dose

* Corresponding author. Centro Singular de Investigación en Tecnoloxías Intelixentes (CiTIUS), University of Santiago de Compostela, 15782, Santiago de Compostela, Spain

E-mail address: nourelislam.boukortt@rai.usc.es (N.E.I. Boukortt).

https://doi.org/10.1016/j.solmat.2025.113943
Received 9 July 2025; Received in revised form 1 September 2025; Accepted 2 September 2025
Available online 5 September 2025
0927-0248/

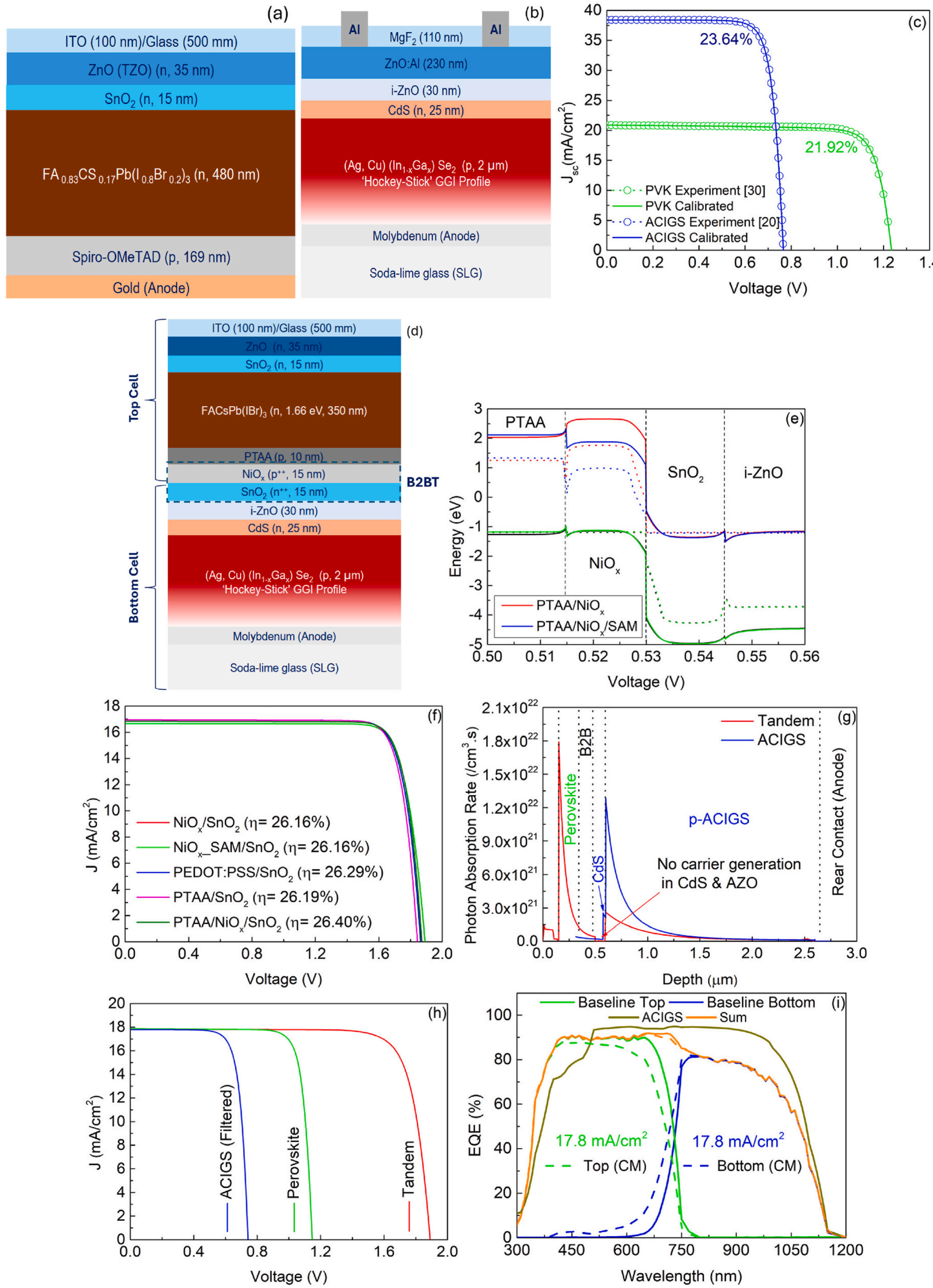

Fig. 1. (a) Schematic structure of the reference perovskite single-junction solar cell. (b) Schematic structure of the reference ACIGS single-junction solar cell. (c) J–V curves for the calibrated perovskite and ACIGS solar cells, compared with experimental data [20]. (d) Stacking structure of the two-terminal (2T) perovskite/ACIGS tandem solar cell (TSC). (e) Energy band diagram of the PTAA/NiO_x/SnO_2 tunneling recombination junction (TRJ), illustrating the band-to-band tunneling (B2BT) mechanism. (f) J–V curves for different materials at the TRJ. (g) Photon absorption rates across the tandem solar cell (red line) and the ACIGS single-junction solar cell (blue line) under AM 1.5 spectrum illumination. (h) J–V characteristics of the perovskite single-junction, ACIGS single-junction, and thin-film perovskite/ACIGS tandem solar cell after the current matching process. (i) EQE spectrum of the subcells and tandem solar cell before and after the current matching process. (For interpretation of the references to colour in this figure legend, the reader is referred to the Web version of this article.)

of 2×10^{12} p^+/cm^2 as well as their excellent performance under weak light [17]. Recent advances, including a stepwise solvent-annealing strategy for wide-bandgap $(CsFAMA)Pb(IBr)_3$ perovskite films, have enabled semitransparent PSCs with a bifaciality factor of 92.2 % and 4-T tandem PSC/CIGS devices reaching a PCE of 29.36 %, surpassing many previously reported tandem devices and confirming their promise for efficient, stable, and cost-effective tandem photovoltaics [18,19]. Despite still trailing the highest-performing perovskite/Si tandems, perovskite/CIGS TSCs now achieving up to 29.9 % PCE in 4T and 24.2 % in 2T configurations continue to show strong potential, especially in flexible monolithic formats, which currently reach 23.64 % PCE and are poised to enable the next generation of high-performance thin-film solar technologies [8,17–19].

CIGS ($Cu(In,Ga)Se_2$) is a well-established photovoltaic technology, serving as an ideal bottom cell in perovskite/CIGS tandem solar cells [20,21]. Recent advancements include the development of $AgCu(In,Ga)Se_2$ (ACIGS), where the incorporation of silver (Ag) during the CIGS growth process leads to its homogeneous distribution throughout the absorber layer [20–24]. This results in enhanced crystallinity, larger grain sizes, and improved optoelectronic performance [20,24]. It has achieved a power conversion efficiency (PCE) of 23.6 % using a 'hockey-stick' GGI (Ga/(In + Ga)) profile [20]. ACIGS enables precise bandgap tuning (1.0–1.7 eV) through control of the Ga/(In + Ga) ratio, facilitating optimal bandgap alignment with perovskite top cells for enhanced solar spectrum utilization [20]. Moreover, ACIGS solar cells demonstrate robust stability, further supporting their commercial viability as a promising evolution of conventional CIGS technology [24].

This paper presents a numerical investigation of 2T perovskite/ACIGS tandem solar cells using Silvaco TCAD tools, offering detailed insights into the device's electrical and optical behavior. The two subcells are connected via band-to-band tunneling (BTBT), a well-established mechanism for enabling efficient monolithic tandem integration [25]. Once BTBT is achieved, the primary factor governing current transport becomes the doping density at the interface. A major challenge in optimizing tandem performance, particularly the fill factor (*FF*) and open-circuit voltage (V_{oc}), lies at the ETL/perovskite and perovskite/HTL interfaces. Imperfections at these junctions often resulting from suboptimal deposition conditions or lack of interfacial engineering can introduce recombination losses, which degrade overall device efficiency without necessarily improving the short-circuit current density (J_{sc}). To address key challenges in perovskite/ACIGS tandem solar cells, this study focuses on optimizing perovskite materials, their electrical and optical properties, and thickness for improved bandgap and current matching. It also examines the impact of perovskite bulk defects on performance and analyzes interface quality at the ETL/perovskite and perovskite/HTL interfaces by varying interface defect density (D_{it}) and surface recombination velocity (*SRV*). The yearly energy yield of PV devices and their performance are strongly influenced by irradiance and operating temperature [26–29]. Therefore, the optimized tandem solar cells were evaluated under varying temperature fluctuations and light intensities, demonstrating improved temperature coefficients for voltage, current, and power compared to the reference model. Through these analyses, the simulations provide valuable insights into the factors influencing overall device performance, offering guidance for designing higher-efficiency tandem solar cells. Additionally, the study includes a comparative analysis of photovoltaic efficiency records to contextualize and validate the proposed approach. This work advances the understanding and development of high-performance perovskite/ACIGS tandem solar cells.

2. Device structure

In this numerical study, the subcells were individually designed, tested, and calibrated using experimental data from Keller et al. and Luo et al. [20,30] to validate the numerical models for subsequent tandem cell investigations. Calibration was performed by first using available material and device properties from experimental data [20,30], and then adjusting parameters such as carrier mobilities, density of states, bulk defect densities, interface defect densities, interface recombination velocities, and contact resistance until the simulated current density–voltage (J–V) and external quantum efficiency (EQE) characteristics closely matched the reported measurements [20,30]. These results are illustrated clearly in the supplementary material (Figs. S1 and S2). Silvaco–Atlas software has been used to simulate the solar cells under investigation. For carrier statistics, the Fermi model is enabled instead of the default Boltzmann model. The Fermi distribution describes the probability of an electron occupying a given energy state, with the probability dependent on the Fermi level, temperature, and energy state. Additionally, a bandgap narrowing (BGN) model is implemented, providing an analytical expression that describes how the semiconductor bandgap varies with doping concentration. To describe charge-carrier mobility, we employed Thomas's analytic model (ANALYTIC), a concentration-dependent mobility model that also accounts for temperature dependence. Carrier recombination is modeled using the CONSRH framework, which links the Shockley–Read–Hall lifetime to carrier density, thereby accounting for the impact of defects, impurities, and free-carrier levels on collection efficiency. Additionally, the TRAP.TUNNEL option enables trap-assisted tunneling, altering how trap states and quantum-mechanical tunneling are treated in the simulation [31]. Fig. 1(a) illustrates the schematic of the theoretical perovskite single-junction solar cell model. The perovskite layer has the composition $FA_{0.83}Cs_{0.17}Pb(I_{0.8}Br_{0.2})_3$, which corresponds to a wide bandgap of approximately 1.66 eV. The electron transport layer (ETL) and hole transport layer (HTL) are modeled as SnO_2 and Spiro-OMeTAD, respectively. A thin TZO(O) interlayer is included at the SnO_2/ITO interface to simulate the effects of RF magnetron sputtering treatments, which are reported to enhance device stability and reduce hysteresis [30]. The model assumes gold (Au) back contact as the rear electrode.

Fig. 1(b) shows the schematic of a theoretical ACIGS single-junction solar cell model. The ACIGS absorber layer is modeled with a 'Hockey-Stick' GGI profile, resembling that typically obtained via a three-stage co-evaporation process, deposited on a molybdenum (Mo) back contact simulated as sputtered on soda-lime glass (SLG) [20]. To represent improved interface quality, sodium fluoride (NaF) and rubidium fluoride (RbF) layers are included at the Mo/ACIGS and buffer/absorber interfaces, respectively, to account for enhanced electrical properties and reduced recombination losses. CdS and ZnO layers are incorporated as the buffer and window layers, respectively. The front contact is modeled as an aluminum (Al) metal grid, with deposition methods such as thermal evaporation or electron beam evaporation considered for completeness [16]. An antireflection coating (ARC) of magnesium fluoride (MgF_2, 110 nm) is also modeled to simulate its effect on optical performance [16,24,25].

Fig. 1(c) presents the J–V curves for the calibrated perovskite and ACIGS solar cell models, alongside experimental data [20,30]. The results show excellent agreement between the experimental data and the modeled curves for both types of solar cells, confirming the accuracy of the calibration and modeling under standard test conditions (STC).

Fig. 1(d) illustrates the schematic of a perovskite/ACIGS TSC. In the two-terminal (2T) structure, the top cell (absorbing higher-energy photons) is directly fabricated on the bottom cell (absorbing lower-energy photons), connected through a direct band tunneling using band-to-band tunneling (BTBT) model [25,31]. This connection requires both optical and electrical coupling [25]. A recombination layer (RL) was previously used to connect in series the two subcells effectively [8,19]. Indium tin oxide (ITO) is the most commonly used recombination junction (RJ) material in high-efficiency tandem solar cells. However, its high lateral conductivity can amplify the impact of local shunts in the top cell, adversely affecting overall device performance [32]. The material properties used in the perovskite/ACIGS structure were derived from experimental studies and our previous investigations [19,20,23,25]. These values are summarized in the supplementary material

Table 1
Performance parameters of the investigated models.

PV Devices	J_{sc} (mA/cm²)	V_{oc} (mV)	FF (%)	η (%)	Reference
Fabricated Perovskite (1.66 eV)	20.94	1236	81.09	20.89	[30]
Calibrated Perovskite	20.89	1235.68	81.02	20.92	This work
Fabricated ACIGS (1.13 eV)	38.30 (38.50)	767 (763)	80.50 (80.80)	23.64 (23.60)	[20]
Calibrated ACIGS	38.40	766.52	80.78	23.78	This work
Perovskite/ACIGS with RJT (B2BT)	16.83	1870.99	83.77	26.39	This work
Perovskite/ACIGS with series connection ITO (5 nm)	16.12	1876.16	84.60	25.58	This work
Perovskite (Top cell)	19.62	1137.31	82.29	18.37	This work
ACIGS (Bottom cell, Filtered)	16.10	738.70	77.67	9.24	This work

(Tables S1, S2 and S3). The voltage of the TSC ($V_{tandem,\ cell}$) is the sum of the voltages from the subcells (Eq. (1)), while the total current is limited to the lower current of the two subcells [33]. Under strict current matching, the total current density of the 2T tandem cell equals the current density of either subcell (Eq. (2)), and the current density at the maximum power point (MPP) is similar [33].

$$V_{tandem,cell} \approx V_{top,cell} + V_{inter} + V_{bottom,cell} \tag{1}$$

$$J_{tandem,cell} \approx J_{top,cell} \approx J_{bottom,cell} \tag{2}$$

V_{int} represents the voltage drop across the tunneling (or interface, a negative value) resistance that electrically connects the two subcells in the tandem device. Typically, if any subcell in the TSC is damaged, the entire device ceases functioning. While the 2T structure reduces costs and expands application potential, its preparation is more challenging and constrained by the bottom cell [8]. Achieving high efficiency requires innovative design considerations [8]. In the tandem structure shown in Fig. 1(d), Spiro-OMeTAD has been replaced by PTAA due to its high electron mobility, excellent film-forming properties, and lower interfacial recombination rates compared to other HTL materials [32]. This is attributed to better interface quality and defect passivation at the perovskite interface [34,35]. PTAA also offers improved moisture protection [34].

Fig. 1(e) shows the promising energy band alignment between NiO_x (15 nm) and SnO_2 (15 nm). NiO_x can be doped with impurities like Li, Cu, and Ag to modify its electrical properties. Ivona et al. reported that doping NiO_x with Cu and passivating its surface with MeO-2PACz (SAM) suppresses electron trapping, enhances hole extraction, and reduces non-radiative interface recombination [35–37]. However, NiO_x + MeO-2PACz was not used in this study. We have analyzed various HTL materials including NiO_x, NiO_x/SAM, PEDOT:PSS, PTAA, and the bilayer PTAA/NiO_x and their influence on the J–V characteristics of tandem solar cells. As shown in Fig. 1(f), the PTAA/NiO_x/SnO_2 configuration demonstrates superior efficiency compared to the other combinations and has therefore been selected for further investigation. The impact of the HTL's electron affinity on the J–V behavior is illustrated in Supplementary Fig. S3, highlighting its critical role in device performance. Fig. 1(g) shows the simulated photon absorption rates across the tandem cell (red line) and the ACIGS single-junction cell (blue line) under AM 1.5 spectrum illumination. In the bottom cell, there is no absorption in the ZnO and CdS layers, as these photons are absorbed by the top cell. Under filtered illumination, absorption in the space charge region (SCR) is reduced, as seen in Fig. 1(g). The primary difference between filtered and unfiltered photogeneration rates occurs within the first 150 nm from the CdS/ACIGS interface [38]. The maximum

Table 2
Performance parameters of the models investigated after current matching.

PV Devices	J_{sc} (mA/cm²)	V_{oc} (mV)	FF (%)	η (%)
Perovskite/ACIGS T. with RJT (d_{pvk} = 200 nm, B2BT)	18.19	1882.36	80.25	27.48
Perovskite/ACIGS T. with series connection ITO (d_{pvk} = 183 nm, 5 nm)	17.82	1890.55	80.62	27.16
Perovskite (Top cell)	17.85	1147.87	82.54	16.91
ACIGS (Bottom cell, Filtered)	17.79	742.33	77.77	10.27

short-circuits current density increases with a decrease in the bottom cell absorber bandgap; in contrast the maximum open-circuit voltage increases linearly with an increase in the bottom cell absorber bandgap. This tandem solar cell was analyzed and optimized by fitting current–voltage and external quantum efficiency curves. Fig. 1(h) shows the J–V curves of the perovskite, ACIGS, and tandem solar cells after current matching by adjusting the perovskite film thickness [19]. Fig. 1 (i) presents the EQE for both simulated subcells before and after current matching under the AM 1.5G solar spectrum. The output characteristics of the measured and simulated models are detailed in Table 1, while Table 2 presents the output characteristics of the calibrated tandem model after current matching, as referenced in Refs. [20,30]. Both tables illustrate the output characteristics, comparing the interconnection differences between BTBT (p^+/n^+) and via ITO (5 nm) layer. It has been reported that in a 2T tandem device using ITO recombination junction (RJ), reducing the ITO thickness from 20 nm to 5 nm increases the sheet resistance from 5×10^2 Ω/□ to 2×10^3 Ω/□. Despite this increase in sheet resistance, the device exhibits higher shunt resistance, which contributes to an improved V_{oc} and enhanced overall performance [32]. Improvements in both subcells are necessary to progress from the current record efficiency of 24.6 % toward the anticipated 30 % [39]. The top and bottom cells used here have V_{oc} values of 1137.31 mV and 738.70 mV, respectively (see Table 1), while the record perovskite and ACIGS single-junction devices have V_{oc} values of 1235.68 mV and 766.52 mV, respectively. This introduces a total V_{oc} loss of ~130 mV in the tandem device, with experimental results showing nearly 100 mV in V_{oc} loss from the bottom cell alone [30]. To address this, the bandgap of the perovskite absorber must be increased to 1.8 eV, at which the tandem cell should achieve a V_{oc} of 2 V.

3. Results and discussion

The primary objective of this study is to investigate the influence of the top subcell on the overall performance of two-terminal (2T) thin-film tandem solar cells and to identify strategies for enhancing power conversion efficiency through the optimization of key parameters in both the top and bottom subcells. Initially, the electrical and optical behavior of each subcell was simulated independently. Subsequently, the subcells were interconnected in series using a band-to-band tunneling (B2BT) junction to facilitate efficient carrier recombination and ensure current matching across the device [8,9], forming a monolithic 2T tandem configuration. Particular emphasis is placed on the top subcell, a perovskite solar cell (PSC), with a detailed analysis of how its optical properties and charge transport layers affect the overall tandem performance. The simulation models employ a two-dimensional (2D) device architecture, as depicted in Fig. 1, and all simulations were performed under standard test conditions (STC: AM1.5G spectrum, 100 mW/cm² irradiance, and temperature of 25 °C).

A. Optical enhancement

In this section, we investigate the influence of perovskite compositions with varying electrical and optical properties on the performance of tandem solar cells. A common assumption is that increasing the

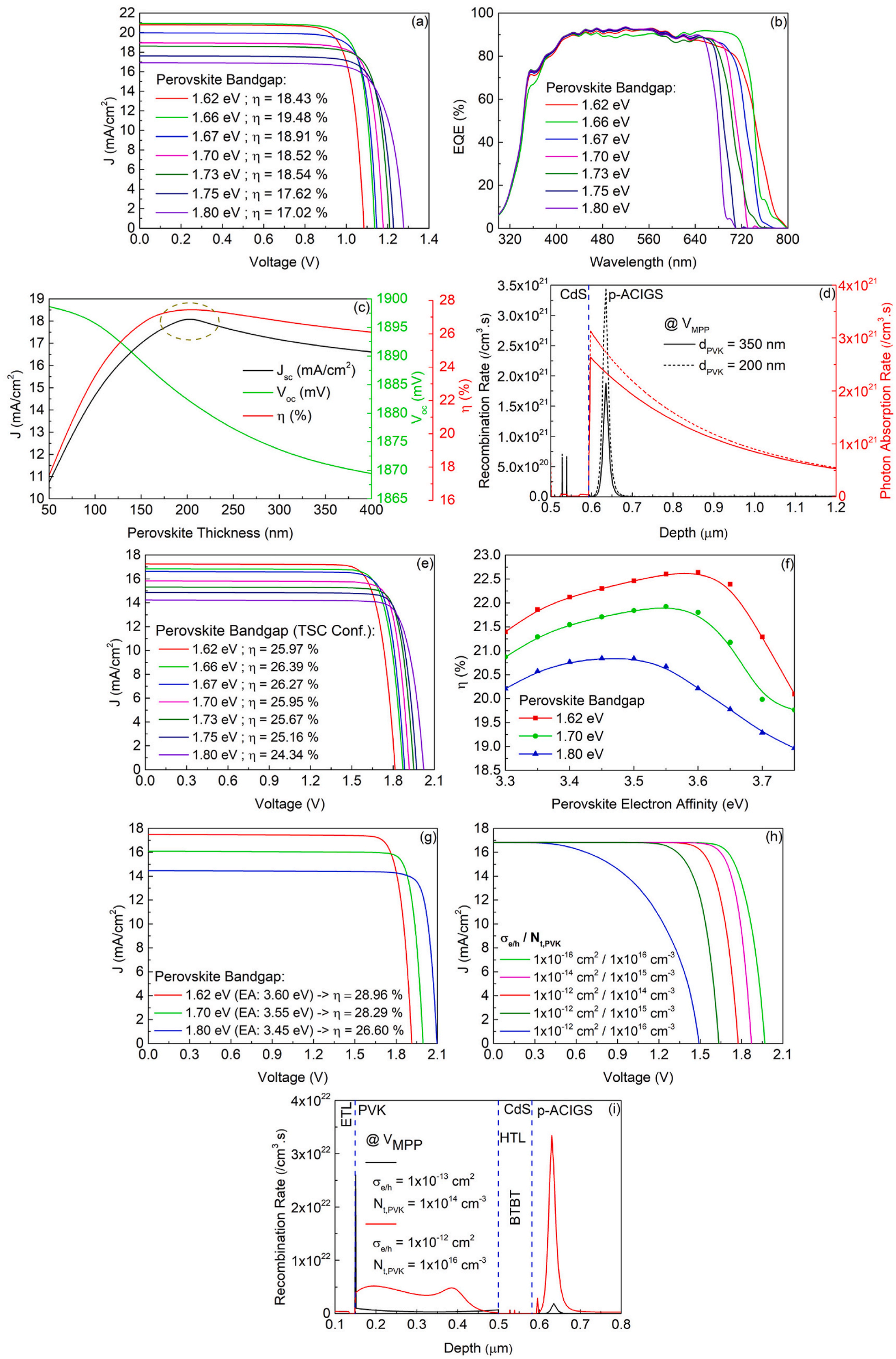

Fig. 2. Performance analysis of perovskite and tandem solar cells: (a) J–V Characteristics. (b) EQE Spectrum. (c) Perovskite Layer Thickness. (d) Recombination and photon absorption rates across the bottom subcell. (e) J–V characteristics of tandem solar cells for different perovskite materials. (f) Efficiency vs. perovskite electron affinity. (g) J–V Characteristics with optimized electron affinity, demonstrating improved performance metrics such as η. (h) Capture cross-section effect on J–V characteristics. (i) Recombination rates across the tandem solar cell.

bandgap of the perovskite layer inherently enhances efficiency. However, this is not universally true, as a higher bandgap can lead to reduced current generation, adversely affecting current matching in two-terminal (2T) tandem configurations. Wide-bandgap perovskites can be engineered by adjusting the iodine/bromine ratio. To enhance both stability and performance, Zhang et al. reported that co-doping with $Pb(SCN)_2$ and PEACl significantly improves wide-bandgap perovskite films [1]. $Pb(SCN)_2$ slows down the crystallization process, leading to films with larger grains and fewer grain boundaries, thereby enhancing film quality. Meanwhile, PEACl promotes the formation of $(PEA)_2PbI_xCl_{4-x}$ at the grain boundaries, which helps to reduce halide phase separation and improve water resistance [1]. These films were tested in a four-terminal (4T) tandem solar cell configuration with silicon, achieving a power conversion efficiency (PCE) of 30.53 % [1]. The perovskite films were deposited using blad coating, a scalable deposition technique [1]. Fig. 2 (a) and (b) present the J–V curves and EQE characteristics for a single perovskite structure, highlighting variations in performance metrics such as fill factor and efficiency, respectively. These results validate the use of appropriate optical properties, with refractive index (n) and extinction coefficient (k) values sourced from PVLighthouse [38]. Notably, the perovskite with a bandgap of 1.66 eV exhibits enhanced light absorption in the 650–725 nm range, primarily due to high-quality interfaces achieved during deposition by Luo et al. [30], which reduce recombination losses and improve charge collection compared to older materials whose properties were based solely on PVLighthouse data [40,41]. Following thickness optimization for the tandem configuration, the optimal perovskite thickness was determined to be within the range of 180–250 nm. This range ensures a balance between photon absorption and charge carrier extraction, leading to matched current densities and minimized recombination losses in the subcells, as illustrated in Fig. 2 (c). It is worth noting that the n, k dataset used for calibration was extracted from relatively thick perovskite films. Since optical constants can vary with thickness due to microstructural differences, crystallinity, and interface quality, this may partly explain the discrepancy between simulated and experimental thickness requirements. While single-junction perovskite devices generally require thicknesses of ~400 nm or more to ensure sufficient absorption [25,30], tandem solar cells impose different optical constraints because light must also reach the bottom cell, thereby shifting the optimum thickness to lower values to absorb only part of the incident spectrum. A thickness of approximately 350 nm was selected to align with experimental feasibility, reflecting the practical limitations encountered in laboratory settings [25]. For the bottom cell, the recombination and photon absorption rates are extracted at the maximum voltage (V_m), as shown in Fig. 2(d). A reduction in the absorber layer thickness decreases the recombination rate in the top cell. However, when the thickness of the top cell is reduced, absorption increases in the bottom cell, leading to enhanced carrier generation in the bottom cell, which in turn results in an increase in the recombination rate in the bottom cell. To assess the influence of bandgap variations on tandem solar cell performance, perovskite materials with different bandgaps were integrated into the tandem structure, as illustrated in Fig. 2(e). Each perovskite was used at a fixed thickness (480 nm) with corresponding optical properties (n, k files). The materials and their bandgaps are as follows: $Cs_{0.15}FA_{0.85}Pb(I_{0.333}Br_{0.667})_3$ (1.62 eV), $FA_{0.83}Cs_{0.17}Pb(I_{0.8}Br_{0.2})_3$ (1.66 eV), $Cs_{0.09}FA_{0.91}Pb(I_{0.25}Cl_{0.75})_3$ (1.67 eV), $Cs_{0.08}FA_{0.92}Pb(I_{0.25}Cl_{0.75})_3$ (1.70 eV), $Cs_{0.1}FA_{0.9}Pb(Br_1)_3$ (1.73 eV), $Cs_{0.08}FA_{0.92}Pb(Cl_1)_3$ (1.75 eV), and $Cs_{0.17}FA_{0.83}Pb(Cl_1)_3$ (1.80 eV) [40,41]. This range of bandgaps allows for systematic evaluation of light absorption and current matching in the tandem architecture. This approach provides valuable insight into how bandgap tuning impacts the power conversion efficiency and fill factor of the tandem device. Fig. 2(e) also presents the FF and η values for tandem architecture incorporating various perovskite compositions. The total absorbed light within the 300–1200 nm spectral range corresponds to a maximum theoretical photocurrent density (J_{ph}) of 46.46 mA/cm^2. For the tandem with a 1.66 eV bandgap perovskite top cell, reflectance losses amount to 7.82 mA/cm^2, reducing the effective maximum photocurrent density. After accounting for optical and parasitic losses, the implied photocurrent contributions are 19.62 mA/cm^2 from the perovskite top cell (J_{top}) and 16.10 mA/cm^2 from the ACIGS bottom cell (J_{bottom}), leading to a combined total of 35.72 mA/cm^2. However, due to the series-connected configuration of the tandem device, the overall photocurrent is limited by the lower-performing subcell here, the ACIGS bottom cell restricting the net photocurrent to 16.10 mA/cm^2. This highlights a substantial current mismatch between the sub-cells, which adversely affects tandem efficiency. To address these losses, we propose a light management strategy that involves adjusting the perovskite absorber thickness to achieve photocurrent matching between the top and bottom subcells. An optimal perovskite thickness of 200 nm was identified, representing a 280 nm reduction from the reference thickness of a single cell [1,25]. This adjustment decreased the absorbed photocurrent in the top cell while increasing the absorbed photocurrent in the ACIGS bottom cell to 18.19 mA/cm^2, a 2.09 mA/cm^2 improvement over the initial value. This enhancement was achieved through band-to-band tunneling. To further mitigate reflectance losses, an additional anti-reflective coating was applied to the front side of the tandem solar cell. A 110-nm-thick MgF_2 layer, a traditional dielectric material widely used for light management in lab-scale solar cells [42] and recommended for minimizing optical losses in tandem configurations [43], was included in our study. The refractive indices of MgF_2 were sourced from Ref. [40]. This modification increased the absorbed photocurrent in both absorbers to 18.37 mA/cm^2, with the perovskite thickness adjusted to 210 nm, a little bit higher than reported in Table 2.

Additionally, to reduce parasitic absorption losses, the thickness of the front transparent contact decreased from 100 nm to 50 nm, resulting in an absorbed photocurrent of 18.58 mA/cm^2 in both absorbers ($d_{PVK} =$ 220 nm). These optical enhancements culminated in a simulated overall efficiency of 28.14 % for the optimized tandem solar cell, surpassing the recent reported numerical work of 26.69 % [25]. While this comparison highlights the potential of the modeled structure, the primary focus is on demonstrating how optical and electrical optimizations can drive significant performance improvements. Achieving optical balance between the top and bottom subcells reduces recombination mechanisms and improves current matching. This optimization led to a 111 mV increase in V_{oc} due to reduced recombination in the top subcell. The selection of the top cell bandgap remains a critical challenge in tandem configurations. Analyzing the impact of different absorber materials on cell efficiency, particularly V_{oc} (influenced by bandgap) and J_{sc} (influenced by refractive index), provides valuable insights.

The electron affinity (χ) of perovskite materials plays a pivotal role in determining device performance. In this study, χ was systematically varied from 3.3 to 3.75 eV for a single perovskite structure to clearly analyze its impact (Fig. 2(f)). The results demonstrate that the optimal electron affinity values for perovskites with bandgaps (E_g) of 1.62 eV, 1.70 eV, and 1.80 eV are 3.6 eV, 3.55 eV, and 3.45 eV, respectively. High-bandgap perovskites were specifically chosen for use as the top cell in tandem configurations to enhance overall efficiency. Through this approach, efficiencies exceeding 28 % were achieved, as depicted in Fig. 2(g). It is noteworthy that electron affinity influences the fill factor not only through energy level alignment but also by modulating the effect of interface defects. Misaligned energy levels can lead to carrier accumulation at interfaces, thereby amplifying recombination losses via existing defect states. Furthermore, the chemical composition and deposition conditions of individual layers play a critical role in determining tandem cell performance. Given that the top subcell is deposited directly onto the bottom cell, any interfacial incompatibility or property mismatch can propagate and affect the overall device efficiency [1,44,45]. This underscores the importance of co-optimizing both subcells as an integrated system rather than as isolated units. In our analysis, we also explored how variations in defect-related parameters such as trap-assisted recombination rates can influence device behavior under different operating conditions.

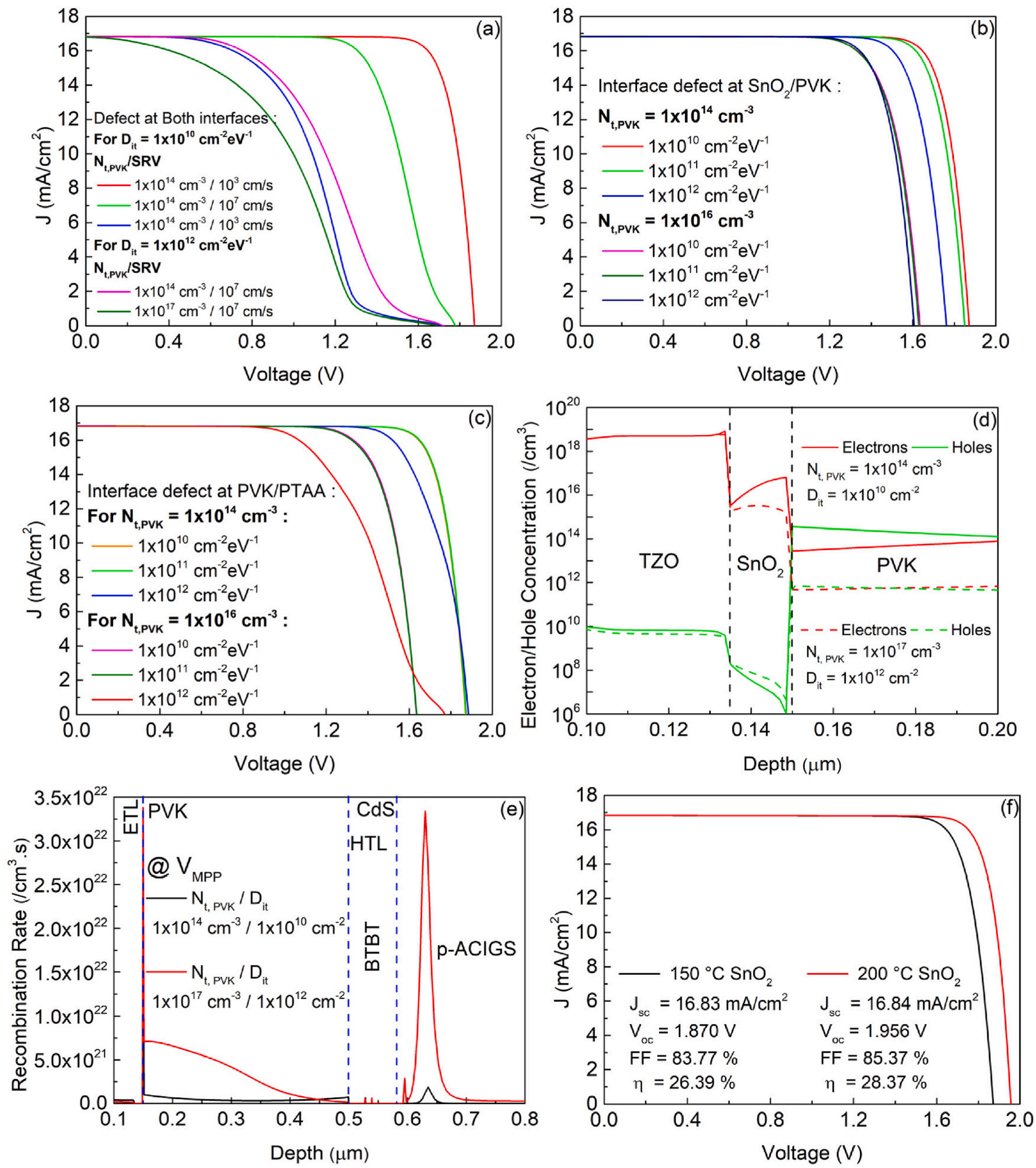

Fig. 3. Performance analysis of tandem solar cells: (a) Impact of SRV at both the ETL/PVK and PVK/HTL interfaces on device performance, evaluated for varying qualities of the perovskite absorber layer. (b) Impact of interface defects at the ETL/perovskite interface. (c) Impact of D_{it} and $N_{t,PVK}$ at the PVK/HTL interface. (d) Electron/hole concentration across the top side of the perovskite structure. (e) Recombination rates across the tandem solar cell. (f) Comparison of J–V characteristics for SnO_2 layers deposited via different processes: spin coating at 150 °C and plasma-assisted atomic layer deposition (ALD) at 200 °C.

Fig. 2(h) illustrates the impact of capture cross-sections on different perovskite defect densities, while Fig. 2(i) presents the recombination rate for two distinct capture cross-sections of perovskite defects. Zhang et al. reported that a high bromine content in perovskites can lead to phase segregation when exposed to light, as well as an increase in defect densities [1]. This significantly reduces V_{oc} and operational instability, driven by enhanced charge carriers trapping at the grain boundaries between regions with different halides, as shown in Fig. 2(h) [1,46]. The issue arises from the energy level differences between the bromide and iodide ions that compose the perovskite film [46,47]. The observed improvement can likely be attributed to the increased grain size and reduced grain boundaries. It is well-known that perovskite grain boundaries are associated with defect states, such as lead vacancies and iodine interstitials. Larger grains help to mitigate defects at these boundaries [46,47].

B. Transport in top subcell

Due to inherent variations in deposition techniques, this study investigates the influence of interface defects on tandem solar cell performance, which may arise from inadequate surface cleaning and/or bulk defects within the absorber layer. Fig. 3 presents a comprehensive performance analysis of the top perovskite subcell and the full tandem structure. Fig. 3(a) illustrates the J–V characteristics under varying

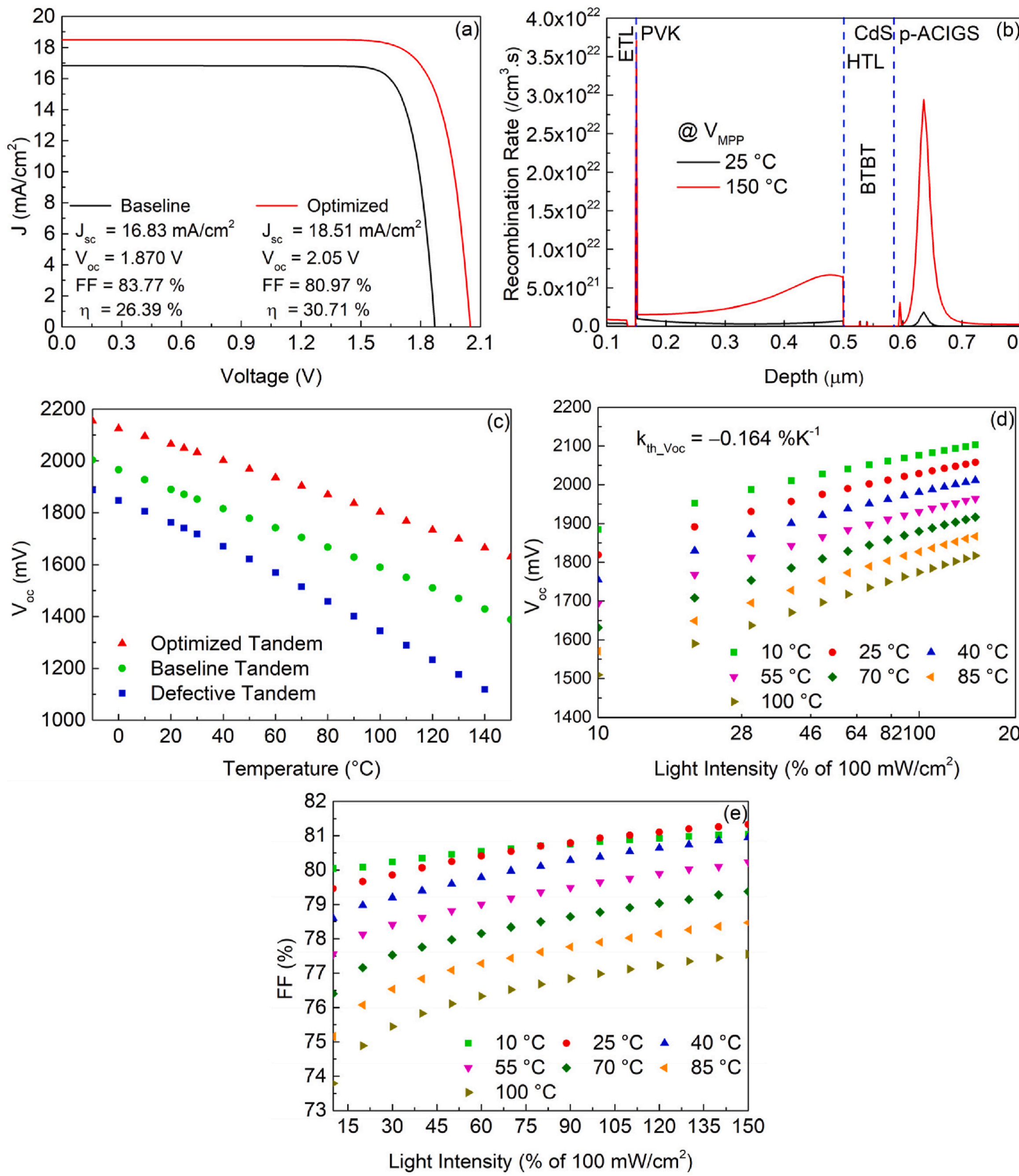

Fig. 4. (a) J–V characteristics at 100 mW cm^{-2} intensity and 25 °C for the tandem devices under test. (b) Recombination rates across the tandem solar cell at two different temperatures. (c) V_{oc} dependence on temperature for different tandem devices, optimized, initial, and defective models. (d) V_{oc} and (e) *FF* dependence on light intensity and temperature.

interface defect conditions, alongside distinct bulk defect levels in the absorber. Interface defects notably impact performance, particularly when perovskite crystallinity is high. Assuming a baseline tandem configuration where optical and electrical properties are not fully optimized significant performance limitations emerge. Under idealized simulation conditions ($D_{it} = 1 \times 10^9$ cm^{-2} eV^{-1}, $SRV = 1 \times 10^3$ cm/s, $N_{t,pvk} = 1 \times 10^{14}$ cm^{-3}), the tandem cell achieves: J_{sc} of 16.83 mA/cm^2, V_{oc} of 1873 mV, *FF* of 83.82 %, and η of 26.44 %. These results are based on wavelength-dependent optical constants (n, k) for each layer, ensuring realistic modeling of photon absorption, reflection, and transmission across the tandem stack thus representing the theoretical performance limit under near-ideal optoelectronic conditions. We began by evaluating tandem performance under defective conditions at both the electron transport layer/perovskite (ETL/PVK) and perovskite/hole transport layer (PVK/HTL) interfaces. In this analysis, we systematically varied both the bulk defect density within the perovskite layer and the surface recombination velocities (SRVs) to assess their combined effects on carrier dynamics, recombination losses, and device efficiency. Under conditions of interface degradation ($D_{it} = 1 \times 10^{12}$ cm^{-2} eV^{-1}, $SRV = 1 \times 10^7$ cm/s, $N_{t,pvk} = 1 \times 10^{14}$ cm^{-3}), we observed a V_{oc} drop of 150 mV and an FF degradation of 37.43 % (Fig. 3(a)). When bulk defect density increases to ~1×10^{17} cm^{-3}, V_{oc} reduces by 380 mV and FF drops by 29 %, suggesting bulk traps become dominant and the relative impact of interface defects diminishes. Fig. 3(b) and (c) isolate the effect of interfacial defects at the SnO_2/PVK and PVK/PTAA interfaces, respectively. These simulations demonstrate how recombination at these interfaces individually influences J_{sc}, V_{oc}, and *FF*. Non-radiative recombination from buried interface defects is a major contributor to performance loss [48,49,50]. As previously reported, trap densities at grain boundaries and interfaces far exceed those within perovskite grains [49,51,52]. Moreover, degradation may be accelerated at the ETL/perovskite interface due to photogenerated carrier transfer processes [9]. Fig. 3(d) displays carrier concentration near the ETL/PVK interface, underscoring how imperfect interfaces degrade V_{oc}. While higher trap densities generally lead to increased recombination, this relationship is not strictly linear. Fig. 3(e) highlights the recombination rate throughout the tandem structure for different interface trap densities at the ETL/PVK interface.

Interfacial defects may originate from premature deposition steps, poor surface treatments, or omission of critical precursors prior to perovskite deposition each contributing to reduced device performance. Since *SRV* is directly influenced by defect states at interfaces, it plays a critical role in solar cell efficiency. Its impact was thoroughly examined in Supplementary Fig. S4, especially for films with high crystallinity but without interfacial additives. In such cases, carriers may be trapped at the interface instead of being efficiently extracted. To investigate this, two bulk defect densities were analyzed: 1×10^{14} and 1×10^{17} cm^{-3}. High *SRV* at the ETL/PVK interface led to a clear reduction in V_{oc} (Fig. S4 (a)), while increased bulk defect density degraded both V_{oc} and *FF*. The PVK/HTL (PTAA) interface showed behavior highly sensitive to the bulk defect density, as evident in Fig. S4(a). At high interface and bulk defect densities, device performance drastically declined, with a V_{oc} reduction of 142 mV, a 50 % drop in *FF*, and efficiency falling from 26.39 % to 10.03 %, a trend corroborated in literature [25]. To capture this behavior, interface trap density varied from 1×10^{11} to 1×10^{12} cm^{-2} in 1×10^{11} cm^{-2} increments, as shown in Fig. S4(b).

On the ETL side, SnO_2 was used as the electron transport layer. Fig. S4(c) demonstrates the sensitivity of performance to interface D_{it}, *SRV*, and $N_{t,PVK}$. These results reinforce the need for high-quality perovskite layers and effective interface passivation. For fabrication, SnO_2 solution was spin-coated at 4000 rpm for 30 s, followed by annealing at 150 °C for 30 min in ambient conditions. A 20-min Ozone-UV treatment was also applied. For comparison, SnO_2 layers deposited at 200 °C (as per [53]) showed enhanced crystallinity and electrical properties. Lower temperature SnO_2 deposition introduces a conduction band offset barrier between SnO_2 and ITO, which impedes electron collection. However, deposition at 200 °C improved ETL performance, increasing tandem FF from 83.77 % to 85.37 % and boosting efficiency from 26.39 % to 28.37 % (Fig. 3(f)). An ideal ETL must exhibit a low work function, and a small conduction band offset at the heterojunction properties achieved with SnO_2 at 200 °C [53,54]. Yet, high-temperature processing remains incompatible with most perovskite materials due to thermal degradation. Nonetheless, these insights guide the optimization of low-temperature ALD SnO_2 processes for enhanced device integration [55].

Lastly, simultaneous variation of ETL/PVK and PVK/HTL interfaces emphasized the importance of interface engineering (Fig. 3(a)). Minimizing interface trap densities ($D_{it} < 10^9$ cm^{-2} eV^{-1}) and maintaining $SRV < 10^3$ cm/s is crucial for sustaining high V_{oc} and *FF*, ultimately achieving tandem efficiencies >26 %.

C. Evaluation of the optimized tandem device

In this section, we evaluate the performance of the numerically optimized perovskite/ACIGS tandem solar cell, focusing on key electrical and optical parameters under ideal and near-ideal interface conditions. The simulation results demonstrate how optimization of defect densities, interfacial properties, and optical absorption contributes to improved V_{oc}, *FF*, and overall *PCE*. Furthermore, the model shows good agreement with reported experimental trends [20,25,30], supporting its validity for predictive analysis and future design optimization. To further improve efficiency, antireflection coating consisting of MgF_2 (110 nm) on top of ITO (50 nm) was employed, enhancing photon absorption. The optical behavior of the MgF_2/ITO antireflection coating was simulated using Silvaco's Ray Tracing method, which calculates reflections and transmissions at interfaces based on Fresnel equations. While this method effectively models photon propagation through complex device geometries, it neglects coherent interference and diffraction effects inherent to thin-film coatings, thus providing an approximate description of the antireflection performance. MgF_2 is typically deposited via ALD [30]. For the top subcell, SnO_2, deposited at 200 °C on the perovskite layer ($E_g = 1.66$ eV, $\chi = 3.6$ eV, and $d_{PVK} = 230$ nm), served as the electron transport layer. The defect parameters were chosen based on experimental lab-scale characterizations, the bulk defect density and capture cross-section of the perovskite were set to 1×10^{14} cm^{-3} and 1×10^{-14} cm^2, respectively, while the defect density at the ETL/PVK and PVK/HTL interfaces were fixed at 1×10^{10} cm^{-2} eV^{-1}. These parameters were applied alongside a "Hockey Stick"-shaped GGI profile (H-S) for the bottom ACIGS absorber. From our previous work, which demonstrated a 5.5 % efficiency improvement through double grading of gallium concentration (grading profile: $x_1 = 0.7$ (Toward back side), $x_2 = 0.35$ (Toward front side), we adopted a similar approach in this study to enhance V_{oc} [19]. By applying the above optimized parameters, we achieved a record efficiency of 30.71 % for the perovskite/ACIGS tandem cell with the H-S profile under standard test conditions. Fig. 4(a) presents the optimized J−V curves for both the initial and optimized tandem solar cells.

In real-world outdoor environments, all solar cells, including tandem architectures, must withstand various conditions, such as humidity, temperature fluctuations, and dust accumulation, all of which can impact performance. The temperature dependence of TSC performance is particularly complex, as it not only influences the individual behavior of the top and bottom subcells but also affects the current-matching condition between them an essential factor determining overall device efficiency. Compared to single-junction photovoltaic technologies, the short-circuit current temperature coefficient of perovskite-based tandem solar cells can be negative, positive, or a combination of both, depending on the incident solar spectrum and the operating temperature range [19, 56,57].

It is well-established that the bandgap of CIGS decreases with increasing temperature, whereas the perovskite bandgap generally shows a slight increase under similar conditions [45,58]. As a result, with rising temperatures, the photocurrent generated by the ACIGS sub-cell tends to increase, while that of the perovskite subcell decreases, leading to a current mismatch relative to the optimized condition at standard temperature. This mismatch in perovskite/CIGS TSCs can significantly contribute to performance degradation under varying thermal environments [45,59]. However, the tunability of the perovskite absorber both in terms of bandgap and thickness offers a pathway to mitigate such mismatches. By preoptimizing these parameters, perovskite/ACIGS TSCs can be engineered to maintain better current matching across a wider range of operating temperatures, thus preserving device efficiency. Despite this, the fundamental mechanisms governing temperature-dependent efficiency losses in tandem devices remain insufficiently understood. Continued research is needed to develop optimization strategies, particularly through precise control of perovskite bandgap and absorber thickness, to ensure stable performance under real-world operating conditions [58]. Temperature variations can increase recombination near the front absorber within diffusion length, as confirmed by recombination profile analysis in the simulation, see Fig. 4(b). To mitigate thermal degradation, numerous strategies, including radiative cooling, have been widely adopted to reduce the actual operating temperature of devices [27]. Nonetheless, despite these advancements, temperature continues to exert a substantial influence on device performance, underscoring the ongoing need for effective thermal management solutions.

The yearly energy yield and performance of photovoltaic (PV) devices are influenced not only by operating temperature but also by solar

Table 3
Temperature coefficients of the investigated models.

Tandem Devices	k_{th_Jsc} (%K^{-1})	k_{th_Voc} (%K^{-1})	k_{th_power} (%K^{-1})
Defective	-3.29×10^{-3}	−0.282	−0.355
Baseline	-2×10^{-3}	−0.209	−0.245
Optimized	-3.85×10^{-6}	−0.164	−0.183

irradiance. Additionally, dust accumulation on the module surface reduces light intensity, further diminishing efficiency. Among the various stress factors affecting device longevity, light exposure remains one of the primary drivers of degradation in perovskite solar cells. Due to the complex interplay of environmental conditions, it is highly unlikely that a single accelerated aging test can reliably predict the outdoor lifetime of PSCs [60]. To assess the impact of temperature and light intensity, we conducted simulations of the tandem cells across a temperature range of −10 to 150 °C and light intensities ranging from 10 to 150 mW/cm^2 (representing 10–150 % of full light intensity) [47]. Fig. 4(c) illustrates the influence of temperature on V_{oc} at a constant irradiation of 100 mW/cm^2. The results reveal that the primary cause of PCE reduction with rising temperature is the decrease in voltage, consistent with the detailed balance limit. In contrast, J_{sc} remains largely unaffected, as shown in Table 3. Based on this analysis, we calculated the temperature coefficients for voltage, current, and power for the tandem devices, which are summarized in Table 3 at 100 mW/cm^2 (100 % light intensity). The optimized tandem structure exhibited minimal drops in PV parameters with increasing temperature, leading to higher efficiency and improved performance in warmer conditions.

As expected, V_{oc} exhibited a logarithmic increase with light intensity across the simulated temperature range (10–100 °C) [61]. A 6 % reduction in FF was observed at low light intensity (10 mW/cm^2), which can be attributed to enhanced carrier recombination under reduced photogeneration conditions [60]. Furthermore, a sample has been tested under realistic outdoor conditions placed on a rooftop performing MPP tracking analysis, submillimeter dots have been seen on bottom cells, indicating CIGS delamination [42]. Addressing these issues would improve *FF* [45,61]. We hypothesize that the notable declines in V_{oc} and *FF* may result from changes in material properties, such as conductivity shifts and energy misalignment. To counteract environmental impacts, solar cells are typically encapsulated with a 3.2 mm thick glass layer and a 500 μm thick encapsulation foil [45]. However, this encapsulation can modify the optical properties of the tandem system, increasing reflection and parasitic absorption in the UV range, which in turn reduces J_{sc}. This work aims to achieve high device efficiency in a relatively short time frame by incorporating insights from recent studies. Our findings have the potential to generate considerable interest in this approach, thereby expanding the scope of research in this field. Table 4 provides a summary of the photovoltaic performance of the investigated models, offering a comparative analysis with recent studies [62–69].

4. Conclusion

This study presents a calibrated numerical analysis of two-terminal perovskite/ACIGS tandem solar cells using Silvaco TCAD, aimed at enhancing device understanding and guiding the optimization of high-efficiency tandem architectures. The electrical and optical characteristics of the individual subcells were calibrated using experimentally fabricated reference devices to ensure realistic simulation outcomes. By integrating a band-to-band tunnel junction and optimizing the ETL (SnO_2 at 200 °C), we significantly reduced interfacial recombination, enhancing V_{oc} and overall device performance. The optimized tandem achieved a simulated PCE of 30.71 %, with J_{sc} = 18.51 mA/cm^2, V_{oc} = 2.05 V, and *FF* = 80.97 %. Additionally, the temperature coefficient improved from −0.245 %K^{-1} to −0.183 %K^{-1}, indicating greater thermal stability. Overall, this work enhances the predictive capability of numerical modeling for tandem solar cells and establishes a robust framework for addressing performance losses associated with interface quality and material selection. By integrating targeted optical and electrical optimization strategies, the study provides actionable design insights for the development of next-generation perovskite/ACIGS tandem photovoltaics with superior efficiency and thermal resilience.

CRediT authorship contribution statement

Nour El I. Boukortt: Writing – original draft, Visualization, Software, Methodology, Investigation, Formal analysis, Data curation, Conceptualization. **Antonio Garcia Loureiro:** Writing – review & editing, Validation, Supervision, Resources, Conceptualization. **Johan Lauwaert:** Writing – review & editing, Validation, Supervision, Resources, Conceptualization.

Consent to participate

The authors consent to participate in this research study.

Table 4
Summary of reported photovoltaic (PV) parameters of perovskite/CIGS tandem solar cells. (*: Certified values).

Tandem Devices	Configuration	J_{sc} (mA/cm^2)	V_{oc} (V)	FF (%)	η (%)	Reference	Year
Experimental studies							
Perovskite/Cu(InGa)Se_2 TSC	2T	11.38	1.509	59.33	10.19	[25]	2024
Perovskite/Cu(InGa)Se_2 TSC	2T	18.00	1.58	76	21.60	[62]	2019
Perovskite/Cu(InGa)Se_2 TSC	2T	19.20	1.68	72	23.3*	[63]	2019
Perovskite/Cu(InGa)Se_2 TSC	2T	14.70	1.77	70	15.90	[42]	2020
Perovskite/Cu(InGa)Se_2 TSC	2T	19.20	1.77	73	24.2*	[45]	2022
Perovskite/Cu(InGa)Se_2 TSC	2T	21.10	1.57	75	24.90	[64]	2022
Perovskite/Cu(InGa)Se_2 TSC	2T	17.70	1.65	62	18.10	[65]	2024
Perovskite/Cu(InGa)Se_2 TSC	4T	13.00	–	–	23.90	[66]	2018
Perovskite/Cu(InGa)Se_2 TSC	4T	–	–	–	29.36	[18]	2025
Perovskite/Cu(InGa)Se_2 TSC	4T	–	–	–	29.90	[67]	2023
Perovskite/Cu(InGa)Se_2 TSC	4T	–	–	–	28.40	[68]	2023
Numerical studies							
Perovskite/Cu(InGa)Se_2 TSC	4T	–	–	–	30.00	[66]	2018
Perovskite/Cu(InGa)Se_2 TSC	2T	17.20	1.85	83.87	26.69	[25]	2024
Perovskite (1.69 eV)/Cu(InGa)Se_2 TSC	2T	18.80	2.00	80.00	30.00	[45]	2022
Perovskite (1.70 eV)/Cu(InGa)Se_2 TSC	2T	19.90	2.01	80.00	32.00	[45]	2022
Perovskite/AgCu(InGa)Se_2 TSC	2T	18.02	2.01	80.51	29.32	[19]	2025
Perovskite/AgCu(InGa)Se_2 TSC	2T	18.10	2.04	82.03	30.26	[69]	2025
Perovskite/AgCu(InGa)Se_2 TSC	2T	18.04	2.03	79.25	29.14	[19]	2025
Perovskite/AgCu(InGa)Se_2 TSC	2T	18.51	2.05	80.97	30.71	This work	

Ethics approval

The authors declare that the submitted manuscript is original. They acknowledge the current review has been conducted ethically, and the final shape of the research has been agreed upon by all authors. No Human Participants and/or Animals were involved while conducting this study.

Availability of data and materials

All data is available on supplementary material.

Funding

No funding was received to conduct this study.

Declaration of competing interest

The authors declare the following financial interests/personal relationships which may be considered as potential competing interests: N/A.

Acknowledgement

The authors declare no competing financial interests.

Appendix A. Supplementary data

Supplementary data to this article can be found online at https://doi.org/10.1016/j.solmat.2025.113943.

Data availability

No data was used for the research described in the article.

References

[1] Z. Zhang, et al., Suppressing halide phase segregation in wide-bandgap perovskite film by co-doping strategy for high-performance and stable perovskite solar cells, Materials Today Physics 37 (Aug. 2023) 101187.
[2] National Renewable Energy Laboratory, Best research-cell efficiency chart. https://www.nrel.gov/pv/cell-efficiency.html.
[3] Y. Huang, et al., Recent advancements in ambient-air fabrication of perovskite solar cells, Exploration 5 (3) (Mar. 2025), https://doi.org/10.1002/exp.20240121.
[4] Y. Luan, et al., Dual-function interface engineering for efficient perovskite solar cells, EcoMat 3 (2) (Feb. 2021).
[5] L. Wu, et al., Resilience pathways for halide perovskite photovoltaics under temperature cycling, Nat. Rev. Mater. (10) (Feb. 2025).
[6] M.Y. Ghannam, J. Poortmans, Interpretation of the degradation and trends in the performance of heterojunction silicon solar cells at low temperature, Sol. Energy Mater. Sol. Cell. 279 (Jan. 2025) 113214.
[7] L.M. Herz, Charge-Carrier mobilities in metal halide perovskites: fundamental mechanisms and limits, ACS Energy Lett. 2 (7) (Jun. 2017) 1539–1548.
[8] L. Zeng, L. Tang, Z. Luo, J. Gong, J. Li, X. Xiao, A review of Perovskite/Copper indium Gallium selenide tandem solar cells, Sol. RRL 8 (21) (Mar. 2024).
[9] M.F. Mohamad Noh, N.A. Arzaee, C.C. Fat, T. Sieh Kiong, M.A. Mat Teridi, A. W. Mahmood Zuhdi, Perovskite/CIGS tandem solar cells: progressive advances from technical perspectives, Mater. Today Energy 39 (Jan. 2024) 101473.
[10] W. Shockley, H.J. Queisser, Detailed balance limit of efficiency of p-n junction solar cells, J. Appl. Phys. 32 (3) (1961) 510–519.
[11] M. Green, E. Dunlop, J. Hohl-Ebinger, M. Yoshita, N. Kopidakis, X. Hao, Solar cell efficiency tables (version 57), Prog. Photovoltaics Res. Appl. 29 (1) (Nov. 2020) 3–15.
[12] M.A. Green, E.D. Dunlop, J. Hohl-Ebinger, M. Yoshita, N. Kopidakis, X. Hao, Solar cell efficiency tables (version 56), Prog. Photovoltaics Res. Appl. 28 (7) (Jul. 2020) 629–638.
[13] Z. Yu, M. Leilaeioun, Z. Holman, Selecting tandem partners for silicon solar cells, Nat. Energy 1 (11) (Sep. 2016).
[14] Erkan Aydın, et al., Pathways toward commercial perovskite/silicon tandem photovoltaics, Science 383 (6679) (Jan. 2024).
[15] Z. Li, et al., Cost analysis of perovskite tandem photovoltaics, Joule 2 (8) (Aug. 2018) 1559–1572.
[16] N.L. Chang, et al., A bottom-up cost analysis of silicon–perovskite tandem photovoltaics, Prog. Photovoltaics Res. Appl. 29 (3) (Oct. 2020) 401–413.
[17] F. Lang, et al., Proton radiation hardness of perovskite tandem photovoltaics, Joule 4 (5) (May 2020) 1054–1069.
[18] D. Chen, et al., A stepwise solvent-annealing strategy for high-efficiency four-terminal Perovskite/Cu(InGa)Se2 tandem solar cells, Mater. Today Energy 49 (Jan. 2025) 101816.
[19] Nour Boukortt, A.G. Loureiro, Johan Lauwaert, Optimizing thin-film tandem solar cells: the impact of bandgap grading in ACIGS subcell on performance, IEEE Trans. Electron. Dev. (Jan. 2025) 1–9.
[20] J. Keller, et al., High-concentration silver alloying and steep back-contact gallium grading enabling copper indium gallium selenide solar cell with 23.6% efficiency, Nat. Energy (Feb. 2024) 1–12.
[21] N. Boukortt, et al., Efficiency improvement of ultrathin CIGS solar cells, Sol. Energy 282 (Sep. 2024), 112935–112935.
[22] N.E. Gorji, U. Reggiani, L. Sandrolini, A simple model for the photocurrent density of a graded band gap CIGS thin film solar cell, Sol. Energy 86 (3) (Mar. 2012) 920–925.
[23] N.E.I. Boukortt, A.G. Loureiro, O.A. Almutairi, Numerical analysis of Ga gradient effects in ACIGS absorbers for high-efficiency tandem solar cells, Opt. Quant. Electron. 57 (3) (Mar. 2025).
[24] V. de, A. Pérez-Rodríguez, Understanding the cell-to-module efficiency gap in Cu (In,Ga)(S,Se)2 photovoltaics scale-up, Nat. Energy 3 (6) (Jun. 2018) 466–475.
[25] P. Procel, et al., Opto-electrical modelling and roadmap for 2T monolithic Perovskite/CIGS tandem solar cells, Solar energy materials & solar cells/Solar energy materials and solar cells 274 (Aug. 2024), 112975–112975.
[26] Maxime Babics, H. Bristow, Anil Reddy Pininti, T.G. Allen, S.D. Wolf, Temperature coefficients of Perovskite/Silicon tandem solar cells, ACS Energy Lett. 8 (7) (Jun. 2023) 3013–3015.
[27] M. Wang, et al., Understanding temperature-induced performance degradation in perovskite/silicon tandem solar cells, Sol. Energy Mater. Sol. Cell. 282 (Jan. 2025) 113393.
[28] T. Du, et al., Light-intensity and thickness dependent efficiency of planar perovskite solar cells: charge recombination *versus* extraction, J. Mater. Chem. C 8 (36) (2020) 12648–12655.
[29] M. Khenkin, et al., Light cycling as a key to understanding the outdoor behaviour of perovskite solar cells, Energy Environ. Sci. 17 (2) (Dec. 2023) 602–610.
[30] M. Luo, et al., Novel cathode buffer layer enabling over 21.6%/20.9% efficiency in wide bandgap/inorganic perovskite solar cells, Nano Energy 121 (Mar. 2024) 109162.
[31] Silvaco International, Atlas User's Manual Device Simulation Software Santa Clara, Silvaco International, 2012.
[32] S. Chozas-Barrientos, et al., Molecular recombination junction for vacuum-deposited Perovskite/Silicon two-terminal tandem solar cells, ACS Energy Lett. 10 (4) (Mar. 2025) 1733–1740.
[33] C. Yan, J. Huang, D. Li, G. Li, Recent progress of metal-halide perovskite-based tandem solar cells, Mater. Chem. Front. 5 (2021).
[34] F.M. Rombach, S.A. Haque, T.J. Macdonald, Lessons learned from spiro-OMeTAD and PTAA in perovskite solar cells, Energy Environ. Sci. 14 (10) (2021) 5161–5190.
[35] D.B. Khadka, Y. Shirai, M. Yanagida, J.W. Ryan, Kenjiro Miyano, Exploring the effects of interfacial carrier transport layers on device performance and optoelectronic properties of planar perovskite solar cells, J. Mater. Chem. C 5 (34) (Jan. 2017) 8819–8827.
[36] Z. Yi, et al., Self-assembled monolayers (SAMs) in inverted perovskite solar cells and their tandem photovoltaics application, Interdisciplinary materials 3 (2) (Feb. 2024) 203–244, https://doi.org/10.1002/idm2.12145.
[37] Ivona Kafedjiska, et al., Advanced characterization and optimization of NiOx:Cu-SAM hole-transporting bi-layer for 23.4% efficient monolithic Cu(In,Ga)Se2-Perovskite tandem solar cells, Adv. Funct. Mater. 33 (34) (May 2023).
[38] Y. Xiong, et al., Recent advances in perovskite/Cu(In,Ga)Se2 tandem solar cells, Materials today electronics 7 (May 2024), 100086–100086.
[39] H.-Z. Berlin, HZB sets new world record for CIGS Perovskite Tandem solar cells. HZB Website, 2021. https://www.helmholtz-berlin.de/pubbin/news_seite?nid=28846&sprache=en&seitenid=1. (Accessed 15 March 2025).
[40] https://www.pvlighthouse.com.au/refractive-index-library.
[41] J. Werner, et al., Complex Refractive Indices of Cesium–Formamidinium-Based Mixed-Halide Perovskites with Optical Band Gaps from 1.5 to 1.8 eV 3 (3) (Feb. 2018) 742–747, https://doi.org/10.1021/acsenergylett.8b00089.
[42] T. Jacobsson, et al., 2-Terminal CIGS-perovskite tandem cells: a layer by layer exploration, Sol. Energy 207 (Sep. 2020) 270–288.
[43] A.A. Said, et al., Sublimed C60 for efficient and repeatable perovskite-based solar cells, Nat. Commun. 15 (1) (Jan. 2024).
[44] V. de, A. Pérez-Rodríguez, Understanding the cell-to-module efficiency gap in Cu (In,Ga)(S,Se)2 photovoltaics scale-up, Nat. Energy 3 (6) (Jun. 2018) 466–475.
[45] M. Jošt, et al., Perovskite/CIGS Tandem Solar Cells: from Certified 24.2% toward 30% and beyond, ACS Energy Lett. (Mar. 2022) 1298–1307.
[46] S. Draguta, et al., Rationalizing the light-induced phase separation of mixed halide organic–inorganic perovskites, Nat. Commun. 8 (1) (Aug. 2017).
[47] X. Shen, et al., Passivation strategies for mitigating defect challenges in halide perovskite light-emitting diodes, Joule 7 (2) (Feb. 2023) 272–308.
[48] N.E.I. Boukortt, Numerical optimization of 0.5-μm-thick Cu (In1-xGax) Se2 solar cell, Optik 200 (Jan. 2020) 163409.
[49] C. Shi, N. Gu, Z. Sun, J. Xiong, P. Du, L. Song, Interface engineering for efficient ETL-free perovskite solar cells via self-assembled bifunctional monolayer, Appl. Surf. Sci. (684) (Nov 2024), 161950-161950.

[50] C. Gong, et al., Stabilizing buried interface via synergistic effect of fluorine and sulfonyl functional groups toward efficient and stable perovskite solar cells, Nano-Micro Lett. 15 (1) (Dec. 2022).

[51] Z. Ni, et al., Resolving spatial and energetic distributions of trap states in metal halide perovskite solar cells, Science 367 (6484) (Mar. 2020) 1352–1358.

[52] M. Luo, et al., Novel cathode buffer layer enabling over 21.6%/20.9% efficiency in wide bandgap/inorganic perovskite solar cells, Nano Energy 121 (Mar. 2024) 109162.

[53] Y. Kuang, et al., Low-Temperature plasma-assisted atomic-layer-deposited SnO2 as an electron transport layer in Planar Perovskite solar cells, ACS Appl. Mater. Interfaces 10 (36) (Aug. 2018) 30367–30378.

[54] Y. Wei, et al., Decreased hysteresis benefited from enhanced lattice oxygen and promoted band alignment with electron transport layer modification in perovskite solar cells, ACS Appl. Mater. Interface (17) (Feb. 2025).

[55] J.H. Won, H. Choi, S.H. Han, B.K. Park, T.-M. Chung, J.H. Han, Polycrystalline and high purity SnO2 films by plasma-enhanced atomic layer deposition using H2O plasma at very low temperatures of 60–90 °C, Vacuum 196 (Nov. 2021) 110739.

[56] Maxime Babics, H. Bristow, Anil Reddy Pininti, T.G. Allen, S.D. Wolf, Temperature coefficients of Perovskite/Silicon tandem solar cells, ACS Energy Lett. 8 (7) (Jun. 2023) 3013–3015.

[57] T. Du, et al., Light-intensity and thickness dependent efficiency of planar perovskite solar cells: charge recombination *versus* extraction, J. Mater. Chem. C 8 (36) (2020) 12648–12655.

[58] M. Wang, et al., Understanding temperature-induced performance degradation in perovskite/silicon tandem solar cells, Sol. Energy Mater. Sol. Cell. 282 (Jan. 2025) 113393.

[59] P. Tockhorn, et al., Three-Terminal Perovskite/Silicon tandem solar cells with top and interdigitated rear contacts, ACS Appl. Energy Mater. 3 (2) (Jan. 2020) 1381–1392.

[60] M. Khenkin, et al., Light cycling as a key to understanding the outdoor behaviour of perovskite solar cells, Energy Environ. Sci. 17 (2) (Dec. 2023) 602–610.

[61] M. Jošt, et al., Perovskite solar cells go outdoors: field testing and temperature effects on energy yield, Adv. Energy Mater. 10 (25) (May 2020) 2000454.

[62] M. Jošt, et al., 21.6%-Efficient monolithic Perovskite/Cu(In,Ga)Se2 Tandem solar cells with thin conformal hole transport layers for integration on rough bottom cell surfaces, ACS Energy Lett. 4 (2) (Jan. 2019) 583–590.

[63] A. Al-Ashouri, et al., Conformal monolayer contacts with lossless interfaces for perovskite single junction and monolithic tandem solar cells, Energy Environ. Sci. 12 (11) (2019) 3356–3369.

[64] A. Ruiz-Preciado, et al., "Monolithic Two-Terminal Perovskite/CIS Tandem Solar Cells with Efficiency Approaching 25%", ACS Energy Lett. 7 (7) (Jun. 2022) 2273–2281.

[65] J. Zheng, et al., Efficient flexible monolithic Perovskite–CIGS tandem solar cell on conductive steel substrate, ACS Energy Lett. (Mar. 2024) 1545–1547.

[66] H. Shen, et al., Mechanically-stacked perovskite/CIGS tandem solar cells with efficiency of 23.9% and reduced oxygen sensitivity, Energy Environ. Sci. 11 (2) (Feb. 2018) 394–406.

[67] H. Liang, et al., 29.9%-efficient, commercially viable perovskite/CuInSe2 thin-film tandem solar cells, Joule 7 (12) (Nov. 2023) 2859–2872.

[68] X. Liu, et al., Over 28% efficiency perovskite/Cu(InGa)Se2 tandem solar cells: highly efficient sub-cells and their bandgap matching, Energy Environ. Sci. 16 (11) (Jan. 2023) 5029–5042.

[69] N.E.I. Boukortt, A.G. Loureiro, O.A. Almutairi, Numerical analysis of Ga gradient effects in ACIGS absorbers for high-efficiency tandem solar cells, Opt. Quant. Electron. 57 (3) (Mar. 2025).